Low Frequency Waterborne Sound Insulation Based on Sandwich Panels With Quasi-Zero-Stiffness Truss Core

Dongwei Wang
School of Aerospace Engineering,
Beijing Institute of Technology,
Beijing 100081, China
e-mail: wangdw@bit.edu.cn

Quan Zhang
School of Aerospace Engineering,
Beijing Institute of Technology,
Beijing 100081, China
e-mail: quan.zhang@universityofgalway.ie

Gengkai Hu[1]
School of Aerospace Engineering,
Beijing Institute of Technology,
Beijing 100081, China
e-mail: hugeng@bit.edu.cn

Due to the negative correlation between pressure resistance and waterborne sound insulation, low-impedance soundproof materials can hardly work in deep water. Here, we propose a new mechanism to circumvent this problem by employing a sandwich panel with designed dynamics quasi-zero-stiffness (QZS) truss cores. The latticed cores are made of programable curved beams, whose shape is carefully designed to meet the demand of both high-pressure resistance and dynamics QZS. An analytical model is developed to evaluate sound transmission of such panel. It is shown that the low-frequency sound insulation performance of the customized panel increases with the hydrostatic pressure and reaches its maximum when the QZS state is triggered. The effective pressure range of the proposed sandwich panel can be further programed by stacking QZS beam lattices of different static load plateaus. The proposed design strategy stems solely from the structural geometry of the curved beams and is therefore materials-insensitive. The linear/inverse relationships between static loading feature and characteristic mechanical properties/geometrical parameters, and the stacking arrangement of lattice bring out the programability of the panel's bearing capacity. The design strategy, together with the established database, provides a feasible approach for underwater sound insulation of equipment subjected to elevated pressures. [DOI: 10.1115/1.4056316]

Keywords: sound insulation, waterborne sound, quasi-zero-stiffness lattice, pressure resistance

1 Introduction

Sound insulation materials are extensively employed in many industrial sectors to insulate unwanted noises, covering aerospace [1–3], transportation [4,5], submarine/ship [6,7], construction [8,9], and many others. A traditional way to reduce sound transmission is to utilize materials of different impedances compared to surrounding medium; a larger impedance contrast will result in better insulation. Accordingly, many high-stiffness (therefore high impedance) materials [10–12] have been proposed for airborne soundproofing. However, they are no longer valid for waterborne sound [13–15], because the impedance of water is of a comparable order to that of common solid materials, such as metals or polymers. Usually, a solid plate with a huge thickness is required to block waterborne sound, particularly for low frequency cases, e.g., for blocking 100 Hz sound by 20 dB, it will need a 2 mm thick steel plate in air, but 6 m thick one in water.

A more practical way to address this issue is to use low-impedance materials containing air-core patterns [16], e.g., the hollow rubber used in submarines [17]. The inner air reduces sharply the equivalent impedance of the rubber, resulting in strong wave reflections in water. The underwater sound insulation performance increases as the air volume fraction with bubble materials as an extreme case [18,19], which almost attends the upper bound for sound insulation of the same thickness. However, the pressure resistance decreases rapidly as the air volume fraction increases [20]. Conventional underwater sound insulating materials are impossible to satisfy simultaneously the requirements of both high impedance mismatch and

pressure resistance, because the strong coupling between modulus and impedance (or static and dynamic modulus/stiffness) of materials prohibits this possibility [15].

Metamaterial technology developed in recent decades enables the realization of unusual properties impossible with traditional materials, through microstructure design [21–24]. Bragg scattering in periodic structures causes destructive interferences of waves with wavelengths comparable to lattice period [25,26], and thus generates bandgaps for insulating waves in relatively high-frequency ranges. Local resonant mechanisms can lead to negative density or modulus in narrow frequency bands and effectively block the corresponding propagating waves [13,14,27,28]. Although multiple resonances have been proposed to widen the bandwidth, the improvement is limited [14]. Both of the above two bandgap-based mechanisms are not able to realize broadband low-frequency sound insulation. Recently, artificial materials with extreme properties have attracted attention to achieve exceptional performances [29–31]. For instance, it is found that the modulus and impedance of anisotropic materials can be decoupled [15]. In addition, pentamode materials with strong anisotropy can achieve simultaneously low impedance and relatively high effective modulus useful for low frequency waterborne sound insulation [15,31]. However, very fine microstructures of these materials are necessary to maintain their extreme properties, which will result in severe stress concentration or even buckling and limit their practical performance under pressure.

Quasi-zero-stiffness (QZS) isolators of high-static-low-dynamic stiffness have been widely studied to achieve ultra-low frequency vibration insulation under static loading [32,33]. The highly nonlinear behavior of these QZS isolators decouples static (secant) stiffness from dynamic (tangent) one, enabling excellent vibration isolation performance without sacrificing their static loading capacity. Traditional QZS isolators utilize a complex combination of positive-stiffness element and negative-stiffness corrector (usually realized through oblique springs [34,35], magnet rings [36,37],
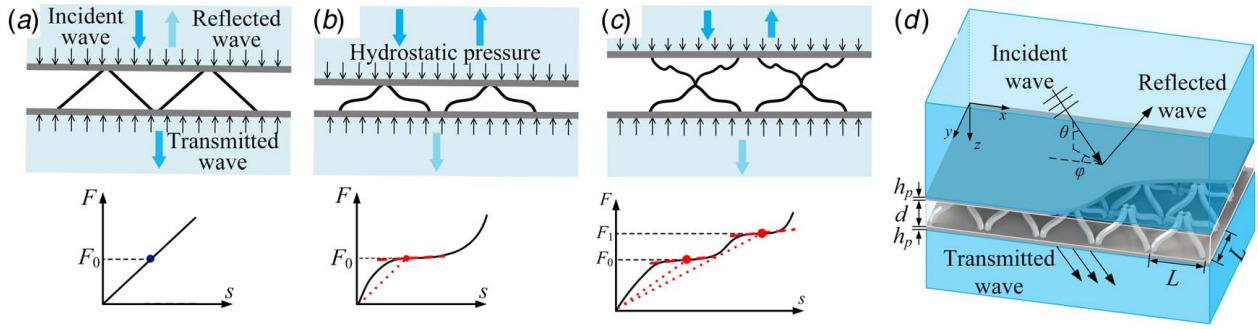
---

[1]Corresponding author.

Fig. 1 Schematic illustrations and the corresponding F-D curve of a latticed sandwich panel under pressure, cored with (a) straight beams, (b) QZS curved beams, (c) stacked QZS curved beams, and (d) the theoretical model of a pyramidal sandwich structure immersed in water

and scissor-like structures [38,39], etc.). Recently, a more compact and concise design strategy has been proposed to achieve desired QZS features, by optimizing the geometric nonlinearity of a monolithic curved beam [40,41]. Here, we will explore the QZS mechanism in insulating low frequency underwater sound for the first time.

In this work, we will design a sandwich panel with tailored dynamics QZS cores, and investigate its sound transmission in a water environment. The rest of the paper is organized as follows. First, in Sec. 2, we will develop an acoustic vibration model of sandwich panel in order to evaluate sound transmission with QZS cores. Second, we will examine a class of tailored QZS beams with customized geometric nonlinearities in order to serve as the core of the proposed sandwich panel. Third, the sound insulation performance of the designed functional sandwich structures with QZS cores will be examined systematically with the proposed model in Sec. 2. Finally, a brief summary is given in the last section.

2 Sound Transmission Model

Due to the strong positive correlation between dynamic and static stiffnesses, traditional sandwich structures with latticed cores of straight beams (see Fig. 1(a)) are not able to satisfy simultaneously the requirements of high impedance mismatch and pressure resistance. Specifically, the straight beams enable the sandwich structure to withstand a high hydrostatic pressure, but at the same time, they also act as a medium for sound transmission. Both the pressure resistance performance and sound transmission property of the sandwich structure are highly related to the beam stiffness. To tackle this problem, we will propose a pressure resistant and sound insulating sandwich panel based on the QZS mechanism, as illustrated in Figs. 1(b) and 1(c). The straight beams in the core are replaced by carefully designed curved beams with tailored force-displacement (F-D) curves to meet pressure resistance and the QZS requirements. The static stiffness of the curved beam at the QZS state (secant slope, highlighted by the dotted red line) is fully decoupled from its dynamic stiffness (tangent slope, highlighted by the dashed red line) (see Fig. 1(b)). Moreover, we can also connect two QZS trusses with different plateaus to program possible static loads, as shown in Fig. 1(c). In order to evaluate the effect of sound insulation by the designed QZS cores, we will develop an acoustic vibration model for this type of panel.

Consider a pyramidal sandwich structure immersed in water. An incident wave impinges upon the top face plate with elevation angle θ and azimuthal angle φ, generating reflected and transmitted waves, as shown in Fig. 1(d). The surrounding water and the air in the core are respectively characterized by (ρ_0, c_0, k_0) and (ρ_a, c_a, k_a) in terms of density, sound speed, and wave number. The material parameters, including density, modulus, and Poisson's ratio, are expressed by ρ_i, E_i, and ν_i, where the subscript $i = p$ for plate and $i = b$ for beam. The thicknesses of the face plates and

the core are denoted by h_p and d, respectively. The unit cells are uniformly distributed along the x- and y-axis with a spacing L.

The plane wave in the incident, core, and transmitted fields can be expressed using velocity potentials in terms of the space harmonic waves as

$$\Phi_{in} = I e^{-j(k_x x + k_y y + k_z z)} + \sum_{kl} R_{nm} e^{-j(k_{xn} x + k_{ym} y + k_z^{nm} z)}$$

$$\Phi_{co} = \sum_{nm} B_{nm} e^{-j(k_{xn} x + k_{ym} y + k_{2z}^{nm} z)} + \sum_{nm} C_{nm} e^{-j(k_{xn} x + k_{ym} y - k_{2z}^{nm} z)} \quad (1)$$

$$\Phi_{tr} = \sum_{nm} T_{nm} e^{-j(k_{xn} x + k_{ym} y + k_z^{nm} z)}$$

where $k_x = k_0 \sin\theta \cos\varphi$, $ky = k_0 \sin\theta \sin\varphi$, and $k_z = \sqrt{k_0^2 - k_x^2 - k_y^2}$ are the components of the incident wavenumber along the corresponding axis. $k_{xn} = k_x + 2n\pi/L$ and $k_{ym} = k_y + 2n\pi/L$ (n and m are integers) denote respectively the Bloch wavenumbers in the periodic structure. k_z^{nm} and k_{za}^{nm} are the wavenumbers along the z-axis in the water and air, respectively. I is the amplitude of the incident wave. R_{nm}, B_{nm}, C_{nm}, and T_{nm} are separately the amplitudes of the corresponding harmonic wave components. The symbol $\sum_{nm}(\cdot)$ represents $\sum_{n=-\infty}^{n=+\infty}\sum_{m=-\infty}^{m=+\infty}(\cdot)$ to alleviate the notation. In all expressions, the time-dependent factor $e^{j\omega t}$ is implicit.

The deflections of the two Kirchhoff face plates can be defined as

$$w_{pi} = \sum_{nm} W_i^{nm} e^{-j(k_{xn} x + k_{ym} y)}, \quad (i = 1, 2) \quad (2)$$

where W_i is the amplitude of the deflection components.

Compared with the plate to beam interaction and the plate to water (or air) interaction, the beam to air interaction in the core is negligible [42]. It is because the direct structural connection is generally far stronger than the fluid-structure one, and the contact area between the plate to water (or air) is much larger than the slender beam to air. Therefore, fluid-structure boundary at the interfaces between the plate and media is only considered. The continuity of normal velocity at the interface yields

$$-\frac{\partial \Phi_{in}}{\partial z} = \frac{\partial w_{p1}}{\partial t}, \quad -\frac{\partial \Phi_{co}}{\partial z} = \frac{\partial w_{p1}}{\partial t}, \quad \text{at } z = 0$$

$$-\frac{\partial \Phi_{co}}{\partial z} = \frac{\partial w_{p2}}{\partial t}, \quad -\frac{\partial \Phi_{tr}}{\partial z} = \frac{\partial w_{p2}}{\partial t}, \quad \text{at } z = d \quad (3)$$

The amplitudes of the wave potentials can be obtained from Eq. (3) as

$$R_{nm} = \begin{cases} I - \omega W_1^{nm}/k_z^{nm}, & n = m = 0 \\ \omega W_1^{nm}/k_z^{nm}, & \text{else} \end{cases}$$

$$B_{nm} = \frac{\omega(W_1^{nm} e^{jk_{za}^{nm}H} - W_2^{nm})}{k_{2z}^{nm}(e^{jk_{za}^{nm}H} - e^{-jk_{za}^{nm}H})}$$

$$C_{nm} = \frac{\omega(W_1^{nm} e^{-jk_{za}^{nm}H} - W_2^{nm})}{k_{2z}^{nm}(e^{jk_{za}^{nm}H} - e^{-jk_{za}^{nm}H})}$$ (4)

$$T_{nm} = \omega W_2^{nm} e^{jk_z^{nm}H}/k_z^{nm}$$

Combining the virtual work by the plates and the beams, the governing equations of the structure are obtained as follows [43]:

$$[D_p(k_{xn'}^2 + k_{ym'}^2) - m_p\omega^2 + \Delta_1]W_1^{n'm'} - \Delta_2 W_2^{n'm'}$$
$$+ \sum_{nm}[\Delta_3 W_1^{nm} - \Delta_4 W_2^{nm}] = \begin{cases} 2j\rho_0 I, & n = m = 0 \\ 0, & \text{else} \end{cases}$$

$$[D_p(k_{xn'}^2 + k_{ym'}^2) - m_p\omega^2 + \Delta_1]W_2^{n'm'} - \Delta_2 W_1^{n'm'}$$ (5)
$$+ \sum_{nm}[\Delta_3\varepsilon_2 W_2^{nm} - \Delta_4\varepsilon_2 W_1^{nm}] = 0$$

where $D_p = E_p h_p^3/12(1 - \nu_p^2)$ is the face plate's flexural stiffness, $m_p = h_p\rho_p$ is the plate's mass per unit area, $\Delta_1 = j\omega^2\rho_0/k_z^{n'm'} + \omega^2\rho_a\cot(k_{za}^{n'm'}d)/k_{za}^{n'm'}$, $\Delta_2 = \omega^2\rho_a/k_{za}^{n'm'}\sin(k_{za}^{n'm'}d)$, $\Delta_3 = 4(K - 2m_b\omega^2 + K_{rx}k_{xn'}k_{xm} + K_{ry}k_{ym'}k_{yn})/L^2$, m_b is the beam's mass, $\Delta_4 = 4(K + K_{rx}k_{xn'}k_{xm} + K_{ry}k_{ym'}k_{yn})\varepsilon_1(-1)^{n+m}/L^2$, $\varepsilon_1 = \cos(k_x L/2)\cos(k_y L/2)$, and $\varepsilon_2 = (-1)^{n'+m'-n-m}$. K, K_{rx}, and K_{ry} are the compressive and rotational dynamic stiffnesses of the beam. For a classic oblique straight beam in pyramidal sandwich core, which has a length of l_b, cross section $w_b \times h_b$ (width × thickness), elevation angle θ_b, and azimuthal angle φ_b [43]

$$K = \frac{E_b A_b l_b^2 \sin^2\theta_b + 12E_b I_b \cos^2\theta_b}{l_b^3}$$

$$K_{rx} = K_{ry} = \left[(1 + 3\sin^4\theta_b)\frac{E_b I_b}{l_b} + \frac{\sin^2\theta_b\cos^2\theta_b}{4}E_b A_b l_b\right]\cos^2\varphi_b$$ (6)

where E_b, A_b, and I_b are Young's modulus, the cross-sectional area, and the second moment of inertia, respectively. For our designed QZS curved beams, their stiffness can be determined by the tangent slope of the F-D curve.

The transmission coefficient τ is defined as the ratio of the transmitted sound power to the incident sound power to evaluate sound transmission, as [12]

$$\tau = \frac{\sum_{nm}|T_{nm}|^2 \text{Re}(k_z^{nm})}{|I|^2 k_z}$$ (7)

Sound transmission loss (STL) is then customarily defined as the inverse of the power transmission coefficient τ in decibel scale

$$\text{STL} = 10\log_{10}(1/\tau)$$ (8)

It has been found that a softer sandwich core has better underwater sound insulation but lower pressure resistance, resulting from the strong coupling between the modulus and impedance [43]. In the following, we will investigate the use of a high-static-low-dynamic stiffness core, consisting of optimized curved beams, to break such coupling between modulus and impedance.

3 Design of Quasi-Zero-Stiffness Truss Cores

In this section, we will design a truss core with dynamic QZS property. To this end, a curved beam lattice will be designed to have the required F-D curve. The curved beams at the QZS state can simultaneously support pressure and block wave propagation. We will demonstrate in the following that the soundproofing property of the sandwich panel with the designed QZS truss core can approach that of an ideal air-core structure, which has an excellent underwater sound insulation performance.

The QZS beams are designed by the optimization method proposed in Ref. [40]. As shown in Fig. 2(a), the curved beam to be designed is enclosed in a rectangular design space of sides l and d, respectively. A vertical displacement is applied on the top end of the beam, and the motions of both ends in the horizontal direction are constrained, as shown in the figure. Its shape is defined by a non-uniform rational B-spline (NURBS [44]) with the control points P_i and the weight coefficients w_i [40]. Details are listed in Appendix A. A genetic algorithm in MATLAB live linked with COMSOL Multiphysics is used to optimize the shape of the QZS beams. The deformation and reaction forces are calculated by using the Beam Interface with Timoshenko formulation. The curved beam is meshed to about 90 beam elements, and MUltifrontal Massively Parallel sparse direct Solver (MUMPS) is selected as the solver to obtain the geometric nonlinear responses. Note that geometric nonlinearity is considered in the finite element method. For the polyamide (PA) materials used in the optimization, we set the density $\rho_b = 1110$ kg/m³, Poisson's ratio $\nu_b = 0.3$, and Young's modulus $E_b = 2.72$ GPa. The side lengths of the design space of the curved beam are $l = 20$ mm and $d = 15$ mm. Accordingly, the endpoint coordinates of the beam are $P_1 = [0, 0]$ and $P_6 = [l, d]$.

The curved beam with a constant reaction force of 3 N at the QZS state is designed using the optimization method, and the corresponding geometry is illustrated in Fig. 2(a). Its geometry parameters are listed as follows: $P_2 = [0.129l, 0.465d]$, $P_3 = [0.441l, 0.504d]$, $P_4 = [0.574l, 0.345d]$, $P_5 = [0.846l, 0.534d]$, $w_1 = 0.766$, $w_2 = 3.268$, $w_3 = 4.113$, $w_4 = 0.570$, $w_5 = 2.642$, $w_6 = 4.958$, the side lengths of cross section are respectively $h_b = 0.62$ mm and $w_b = 9.47$ mm. A curvature fitting is performed to ensure the smoothness of the beam for further fabrication. The F-D curves
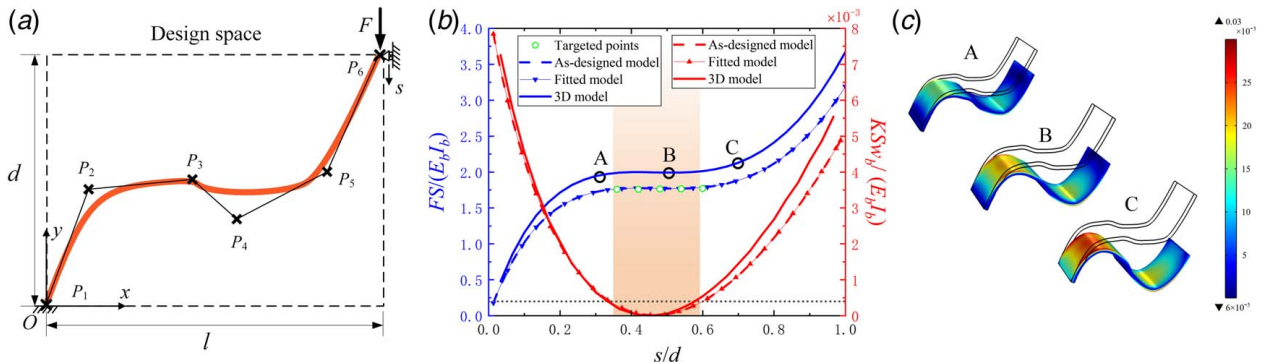

Fig. 2 (a) Schematic diagram of the design space and the optimized beam shape, (b) the force-displacement and stiffness curves of the as-designed, fitted, and 3D solid beams, and (c) deformation and strain color maps at specific loading points
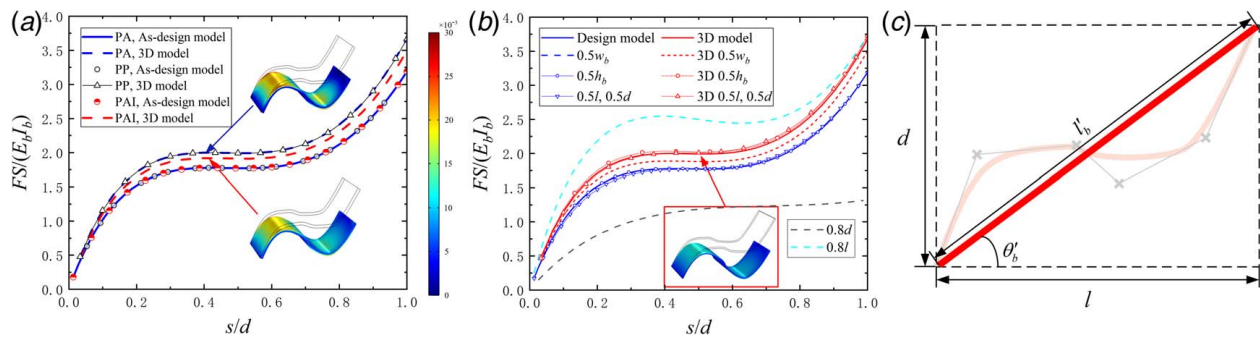
Fig. 3 *(a)* The normalized force-displacement curves corresponding to different constitutive materials, *(b)* the influence of geometric parameters on the normalized force-displacement curves, and *(c)* the reference straight beam corresponding to the optimized curved beam

of the as-designed and fitted beams are shown in Fig. 2(*b*), both almost coincide and pass through the target QZS points marked by the green circles, as required. The reaction force is normalized by $E_b I_b / S$, where S $= ld$ is the area of the design space. In addition, a 3D model of the fitted beam is also built to validate the design method. Its F-D curve is also plotted by the blue solid line in Fig. 2(*b*), exhibiting the desired QZS feature. The difference in the plateau force is due to the Beam Interface simulation in COMSOL—which is close to the plane stress problem—cannot perfectly match the response of a 3D beam with a relatively large out-of-plane thickness [40]. The U-shaped red curves in Fig. 2(*b*) depict the normalized equivalent stiffness. Approximately, we can set 5% of the maximum stiffness as a threshold to define the QZS region, and the resulting normalized displacement range of the desired QZS region is about $s/d = [0.33, 0.58]$. The deformed shapes of the 3D solid beam at three specific loading points (marked by A, B, and C, corresponding to $s/d = 0.3$, 0.5, and 0.7, respectively) are shown in Fig. 2(*c*), with the color map representing the maximum principal strain. The maximum strain is within 3% (which is quite small for polyamide), indicating the feasibility of using a linear elastic constitutive relation in the simulation.

The reported QZS feature is mainly due to the curvature distribution of the beam (P_i in Fig. 2(*a*)), which approximately defines the intrinsic quality of the beam, $E_b I_b / S$. Therefore, the normalized force $FS/(E_b I_b)$ will roughly keep constant unless the curvature varies. To demonstrate it, we change the constitutive material from PA to polypropylene (PP, $\rho = 900$ kg/m³, $\nu = 0.4$, and E $= 1.4$ GPa) and to polyamide imide (PAI, $\rho = 1400$ kg/m³, $\nu = 0.3$, and E $= 9$ GPa), and calculate the corresponding compressive responses. As shown in Fig. 3(*a*), the F-D curves of the as-designed beams with different materials almost overlap; Poisson's ratio may lead to some discrepancies between the F-D curves of the as-designed and 3D beam models. In addition, Fig. 3(*b*) displays the influence of geometric parameters on the normalized F-D curve. One can see that, when the beam's cross-sectional size is changed (labeled as "$0.5w_b$" and "$0.5h_b$" in Fig. 3(*b*)), or its geometric dimension is proportionally changed, e.g., l and d are reduced proportionately by half (labeled as "$0.5\,l, 0.5d$" in Fig. 3(*b*)), the normalized F-D curve remains almost unchanged. By contrast, disproportionately changing the beam's geometric dimension (labeled as "$0.8d$" and "$0.8l$" in Fig. 3(*b*)) will significantly alter the normalized F-D curve. Quantitatively, the actual reaction force of the optimized curved beam can be expressed in the form of $F = E_b I_b f/S$, where f is a function of s/d. With help of the stiffness of an oblique straight thin beam as expressed in Eq. (6), the corresponding reaction force is derived as $F = 12E_b I_b/l_b^2 \cdot (s/l_b) \cos^2 \theta_b$. Similarly, the reaction force of the optimized curved beam can be rewritten as $F = E_b I_b/l_b'^2 \cdot f(s \cos \theta_b'/l_b')/(\sin \theta_b' \cos \theta_b')$, where l_b' and θ_b' are the length and oblique angle of the equivalent straight beam shown in Fig. 3(*c*). Therefore, the actual reaction force F is proportional to the modulus of the constitutive material and the moment of inertia of the beam's cross section, and inversely proportional to the

design space area. This rule enables us to program the QZS plateau force on-demand by changing the modulus of the constitutive material, the cross-sectional dimensions of the beam, or the design space area without re-optimization. Moreover, for different QZS plateau forces, we perform the optimization by varying aspect ratio (l:d) of the design space, and establishing the corresponding database (see Appendix B). Using the database and the aforementioned rule for modifying the QZS plateau force, practical structures with the desired nonlinear F-D curve can be easily designed.

4 Sound Insulation of Sandwich Structure With Quasi-Zero-Stiffness Truss Cores

4.1 Pyramidal Lattice Structure. The desired QZS curved beam lattice can be utilized for decoupling the dynamic and static stiffnesses of the sandwich structure, thus enabling strong pressure resistance performance and excellent underwater sound insulation property at the same time. To ensure that the curved beam is elastically deformed in a QZS state, the constitutive material is selected by establishing the Ashby diagram for materials selection, focusing on the maximum strain in the elastic state versus Young's modulus, as shown in Fig. 4(*a*). It is found that metals can hardly afford an elastic strain larger than 1%, while the maximum elastic strain of polymers can reach 3–8%. Therefore, a composite material consisting of epoxy matrix and glass fibers (marked by the black star "★" in Fig. 4(*a*)) is chosen as the constitutive material for the designed beam. The parameters of the considered composite material are density of 1600 kg/m³, Young's modulus of 40 GPa, and Poisson's ratio of 0.3, respectively.

Consider the design objective that the pyramidal sandwich structure is able to insulate underwater sounds, while supporting 1 MPa hydrostatic pressure. By consulting the curvature database in Appendix B, the Type II QZS beam (with the geometric parameters $l = 10$ mm, $d = 4.8$ mm, $w_b = 2.5$ mm, and $h_b = 0.8$ mm) is selected to build the core of the sandwich structure. The customized sandwich structure with 1 mm thick aluminum face plates is shown in Fig. 4(*b*). Each unit cell contains four QZS beams, and their ends are staggered on the upper panel to make the unit cell compact and to enhance its pressure resistance performance. The compressive response of the sandwich structure is presented in Fig. 4(*c*). As the deformation increases, the QZS beam will be in contact with the plate, leading to a dramatic increase in the effective stiffness; therefore, sudden hardening phenomena are observed in the F-D curve. The deformed configurations of the unit cell at the two inflection points are illustrated in the insets in Fig. 4(*c*). The beam contacts to the bottom plate (corresponding to the first inflection point), and then contacts to the top one (corresponding to the second inflection point). The seeming "inflection" at 2.5 MPa is due to the change in the pressure scale.

The sound insulation performance of the designed structure with normally incident wave under different hydrostatic pressures can be
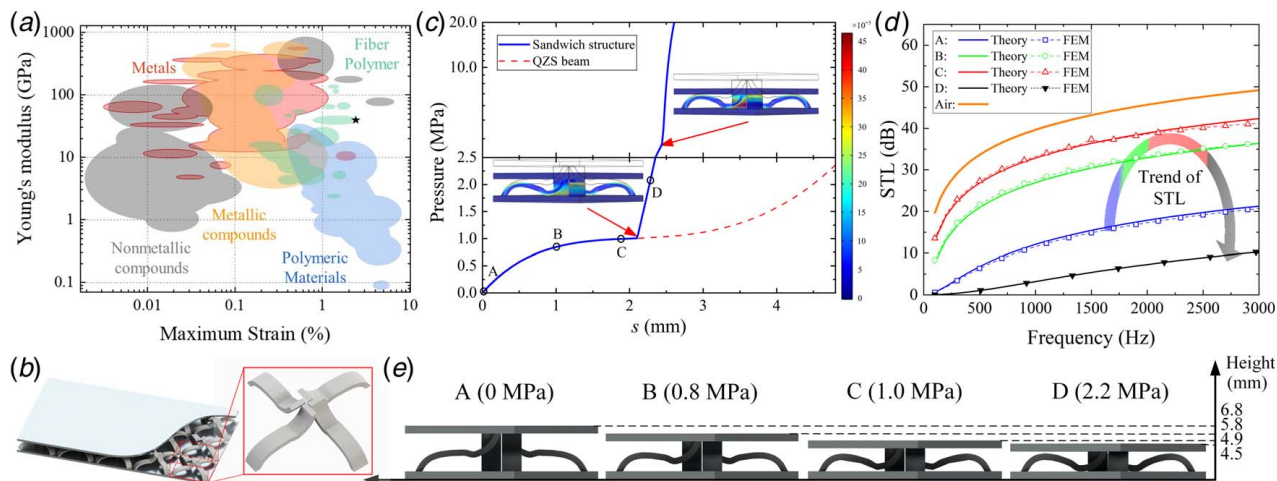
Fig. 4 (*a*) Ashby diagram for materials selection: the plot of the maximum elastic strain versus Young's modulus, (*b*) the pyramidal sandwich structure cored with the QZS beams, (*c*) force-displacement curves of the QZS sandwich panel, (*d*) STL curves, and (*e*) the corresponding deformed states of the sandwich panel under different pressures

calculated by using Eq. (7). The dynamic stiffness of beam in the model under specific pressure is extracted from its F-D curve. Note that the rotational stiffness of the QZS beam (K_{rx} and K_{ry}) has much less influence on STL than the translational one and thus can be neglected [10,12]. For instance, the sound transmission losses, corresponding to A (0 MPa), B (0.8 MPa), C (1.0 MPa), and D (2.2 MPa) (the corresponding deformed states are given in Fig. 4(*e*)), are calculated and compared with finite element simulations, as shown in Fig. 4(*d*). A good agreement is observed, validating the proposed design method and the theoretical model. It is found that the underwater sound insulation performance of the customized structure improves as the pressure increases, and reaches its maximum when the QZS state is triggered. The direct contact between the beams and panels destroys the stiffness decoupling characteristic, and thus deteriorates the insulating property (e.g., state D in Fig. 4(*d*)). The trend of STL resembles an inverted "U" shape as the pressure increases. The effective pressure range is considered as [0.8, 1] MPa, where the customized structure possesses much better underwater soundproofing than the classic latticed sandwich panels with straight high-stiffness beams. Remarkably, the proposed sandwich panel exhibits the best sound insulation

performance under 1 MPa pressure (state C in Fig. 4(*d*)), and the corresponding STL approaches that of a sandwich structure of the same thickness with air-core, which provides an upper bound of sound insulation for the designed QZS structure. Since our design is of elastic range, once the static load is relaxed, the sandwich structure will recover its initial shape.

As depicted in Fig. 3(*b*), disproportionately changing the beam's geometric dimension (reducing the side length l) can cause negative stiffness. To investigate the sound insulation performance of the structure with negative cores, a sandwich panel with 1 mm thickness aluminum face plates and variant Type II QZS composite beam cores (with the geometric parameters $l = 10$ mm, $d = 8$ mm, $w_b = 1.8$ mm, and $h_b = 0.8$ mm) is established. The diagram of the structure cell and the corresponding F-D curves are shown in Fig. 5(*a*). The phenomena of F-D curve are similar to those in Fig. 4(*b*), except a negative-stiffness range locating between the QZS state (point B) and the first inflection point. The sound insulation properties of the negative-stiffness structure in four typical states (points A–D in F-D curve and the corresponding deformed state given in Fig. 5(*c*)) are calculated by the theoretical and numerical models, as shown in Fig. 5(*b*). Remarkably, the structure with
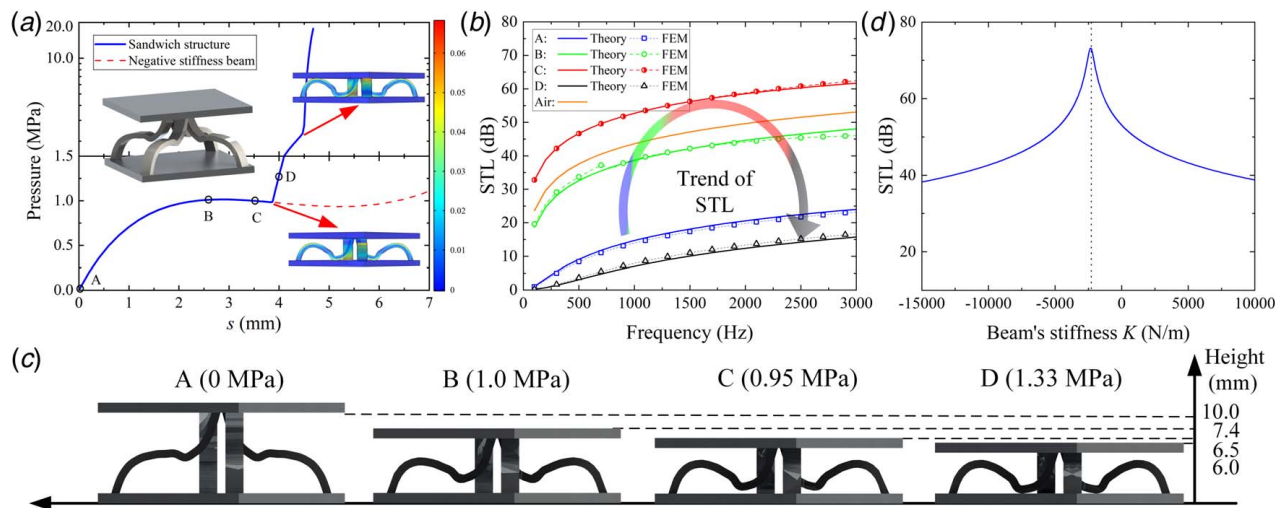

Fig. 5 (*a*) Force-displacement curve of the pyramidal sandwich panel cored with negative-stiffness beams, (*b*) STL of the structure in four typical states, (*c*) the corresponding deformed configurations, and (*d*) the effect of the beam's stiffness on sound insulation performance
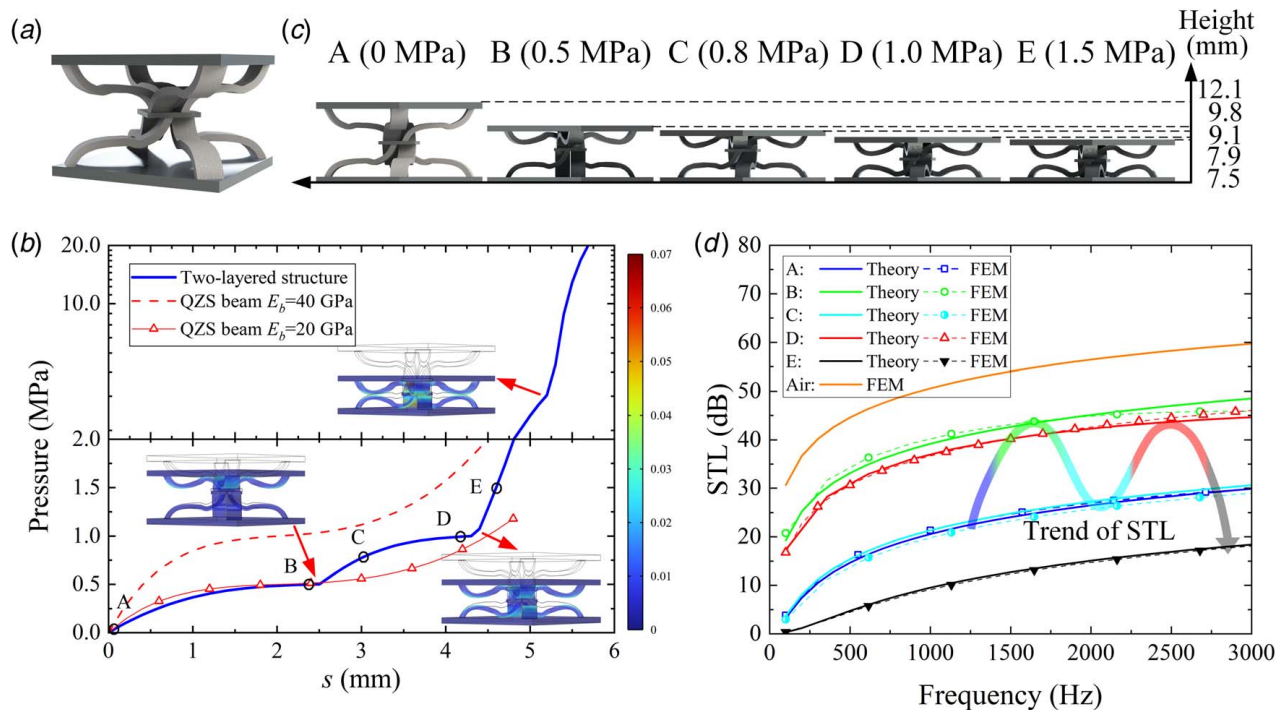
Fig. 6 (a) Schematic diagram of the two-layered pyramidal sandwich panel, (b) its force-displacement curve, (c) the deformed configuration of the two-layered sandwich panel under four typical pressures, and (d) the STL corresponding to these deformed states

negative-stiffness beams can break the upper bound of underwater soundproofing achieved by air-cored sandwich panel. To quantify the effect of negative stiffness, the STL at 3000 Hz of a pyramidal structure with varying beam's stiffness K is calculated and plotted in Fig. 5(d). The peak value of STL occurs when the negative stiffness perfectly counteracts the stiffness of "air spring" $s_{air} = \rho_a c_a^2/d$ [45], i.e., $K = s_{air}L^2/4$. In addition, similar to the positive stiffness, an excessive negative stiffness of beam decreases the STL.

4.2 Programing Static Loads. The effective working pressure range of the proposed structure can be further enlarged by combining curved beams with different QZS plateau forces. To this end, we introduce an hourglass-shaped two-layered pyramidal core, as shown in Fig. 6(a). The curved beams in different layers have different plateau forces at the QZS states. The stacked layers behave like two different springs connecting in series and show two plateaus in the F-D curve of the core. The theoretical model of the layered sandwich panel should be modified by setting $\varepsilon_1 = \varepsilon_2 = 1$ and using m_b to represent the mass of two beams [10]. A simple way to tune the QZS plateau force is by changing the constitutive material. Here, the constitutive material of the beams in the bottom layer is the same as that reported in Sec. 4.1; while the material of the beams in the top layer is replaced by softer polyamide with the parameters $E_b = 20$ GPa, $\rho_b = 1400$ kg/m^3, and $\nu_b = 0.3$. Consequently, the layered structure has two distinct QZS states triggered at 0.5 MPa and 1.0 MPa, respectively, as shown in Fig. 6(b). For reference, the F-D curves corresponding to the two QZS beams are plotted by the red curves in Fig. 6(b). In addition, the deformed configurations at the inflection points corresponding to the contact between the beam and plate are depicted by the insets. First, the beams with the smaller QZS plateau force in the top layer are in contact with the top plate (the first inflection point). Then, the beam in the bottom layer comes into contact with the bottom plate (the second inflection point). Lastly, the beams with the distinct QZS plateau forces contact each other (the third inflection point). Before contact occurs, the response of the layered structure

is dominated by the deformation of the softer QZS beam. However, between the first and second contact points, the deformation of the stiffer QZS beam dominates the response of the layered structure.

The deformed configurations and corresponding STL of the layered structure under five typical pressures—which are marked by A (0 MPa), B (0.5 MPa), C (0.8 MPa), D (1.0 MPa), and E (1.5 MPa)—are shown in Figs. 6(c) and 6(d), respectively. We can see that the panel shows excellent sound insulation performance when the QZS states are triggered (points B and D). The STL trend of the two-layered structure resembles an "M" shape, which is like the combination of two inverted "U" shapes (corresponding to the STL trend of the single-layer sandwich structure studied in Sec. 4.1). The results indicate that the working pressure point and range nearby of the proposed structure can be broadened by a multi-layered design strategy.

5 Conclusions

A new mechanism based on dynamics QZS is proposed to insulate waterborne sound as well as to support pressure. A sandwich structure with QZS cores made of curved beam lattice is proposed to demonstrate this idea. It is shown that the highly nonlinear beam can decouple the static and dynamic properties of the sandwich structure, and thus providing a possibility for such harsh design. A criterion of tuning the QZS feature of the optimized curved beam is brought forward to program the static loading pressure. Based on the established beam curvature database, a pyramidal sandwich panel is customized to insulate underwater sound waves under 1 MPa pressure, its insulating performance is demonstrated by a combination of theoretical analysis model and numerical simulation. To program the supporting pressures, QZS truss cores with different plateau forces can be stacked. The resulting multi-layered core enables QZS states triggered at different pressures, and thus can be used to effectively insulate underwater sound over a wide pressure range. Our work may provide a new route to design pressure resistant waterborne sound insulating materials.
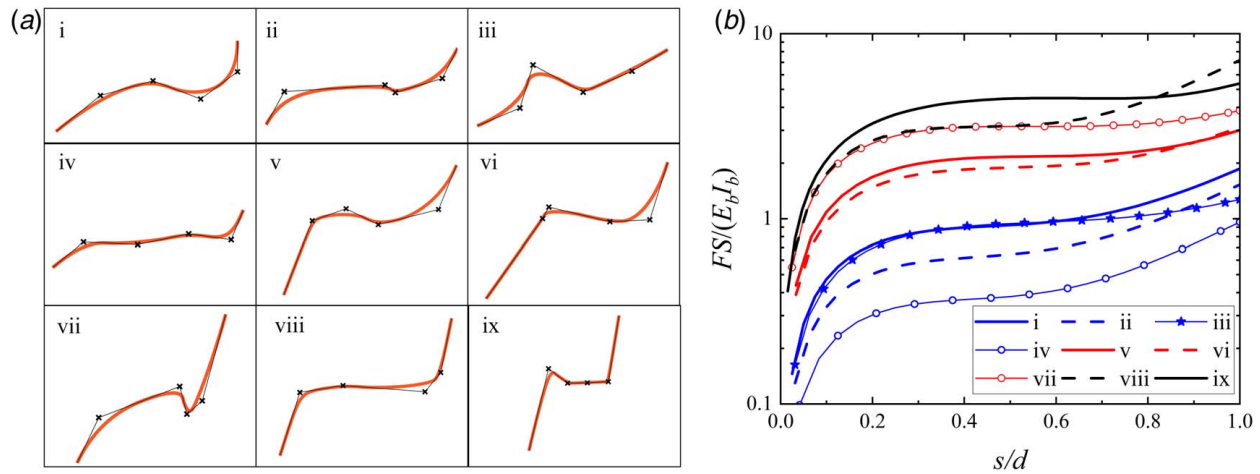
Fig. 7 (*a*) Database of the beam curvatures with different ratios (*l*:*d*) and (*b*) the corresponding normalized force-displacement curve

Table 1   The QZS features of the beam curvatures with different ratios

Type	I	II	III	IV	V	VI	VII	VIII	IX
l:*d*	2:1	5:2	5:2	10:3	4:3	4:3	1:1	5:4	2:3
$FS/(E_bI_b)$	0.90	0.62	0.95	0.36	1.87	2.16	3.15	3.14	4.48
QZS region (*s*/*d*)	[0.40,0.50]	[0.38,0.44]	[0.46,0.63]	[0.33,0.46]	[0.40,0.58]	[0.40,0.67]	[0.37,0.75]	[0.34,0.53]	[0.45,0.80]

Conflict of Interest

There are no conflicts of interest.

Data Availability Statement

The authors attest that all data for this study are included in the paper.

Appendix A: Parametric Characterization of a Curved Beam by NURBS

The shape of a curved beam can be defined by a NURBS [44] with the control points P_i and the weight coefficients w_i as

$$X(\xi) = \frac{\sum_{i=1}^{6} N_{i,p}(\xi)w_i}{\sum_{j=1}^{6} N_{j,p}(\xi)w_j} P_i \qquad (A1)$$

where X denotes a point located on the beam's central axis, $P_i = [P_{ix}, P_{iy}]$ are the coordinates of the ith control points, $N_{i,p}(\xi)$ is the B-spline basis functions, p denotes the degree of the spline basis functions. The detailed expressions of $N_{i,p}(\xi)$ with quadratic polynomial ($p = 2$) and ξ space $[0,0,0,0.3,0.5,0.7,1,1,1]$ are given below [40].

$$N_{i,0}(\xi) = \begin{cases} 1 & \xi \in [\xi_i, \xi_{i+1}) \\ 0 & \text{otherwise} \end{cases}$$

$$N_{i,0}(\xi) = \frac{\xi - \xi_i}{\xi_{i+p} - \xi_i} N_{i,p-1}(\xi) + \frac{\xi_{i+p+1} - \xi}{\xi_{i+p+1} - \xi_{i+1}} N_{i+1,p-1}(\xi)$$

$$(A2)$$

where P_1 and P_6 are constant and fixed at the corner of the design space. P_2–P_5 and w_i are the design variables. The design objective is to minimize the global error $R = \zeta \sum_i^n |F_i - F_i^{tar}|/F_i^{tar}$ between the actual and the desired forces at some specific displacements, where F_i and F_i^{tar} denote respectively the actual and target forces at the ith displacement point. To avoid the negative stiffness, the coefficient $\zeta = 1$ when $F_i < F_{i+1}$, while $\zeta = 100$ when $F_i > F_{i+1}$.

Appendix B: Database of Quasi-Zero-Stiffness Beam Curvature With Different Ratios of Design Space

The QZS features and the F-D curves of optimized beam curvatures with different ratios (Fig. 7) are listed in Table 1. The table shows that the bearing capacity $FS/(E_bI_b)$ generally increases as the ratio l:d decreases. The slimmer beam curvature affords the larger pressure.

References

[1] Georgiadis, S., Gunnion, A. J., Thomson, R. S., and Cartwright, B. K., 2008, "Bird-Strike Simulation for Certification of the Boeing 787 Composite Moveable Trailing Edge," Compos. Struct., **86**(1–3), pp. 258–268.

[2] Mead, D., 1996, "Wave Propagation in Continuous Periodic Structures: Research Contributions From Southampton, 1964–1995," J. Sound Vib., **190**(3), pp. 495–524.

[3] Shen, C., Xin, F., Cheng, L., and Lu, T., 2013, "Sound Radiation of Orthogonally Stiffened Laminated Composite Plates Under Airborne and Structure Borne Excitations," Compos. Sci. Technol., **84**, pp. 51–57.

[4] Petrone, G., D'Alessandro, V., Franco, F., and De Rosa, S., 2014, "Numerical and Experimental Investigations on the Acoustic Power Radiated by Aluminium Foam Sandwich Panels," Compos. Struct., **118**, pp. 170–177.

[5] Talebitooti, R., and Zarastvand, M., 2018, "The Effect of Nature of Porous Material on Diffuse Fifield Acoustic Transmission of the Sandwich Aerospace Composite Doubly Curved Shell," Aerosp. Sci. Technol., **78**, pp. 157–170.

[6] Yin, X., Gu, X., Cui, H., and Shen, R., 2007, "Acoustic Radiation From a Laminated Composite Plate Reinforced by Doubly Periodic Parallel Stiffeners," J. Sound Vib., **306**(3–5), pp. 877–889.

[7] Sorokin, S. V., 2000, "Vibrations of and Sound Radiation From Sandwich Plates in Heavy Fluid Loading Conditions," Compos. Struct., **48**(4), pp. 219–230.

[8] Hongisto, V., 2000, "Sound Insulation of Doors—Part 1: Prediction Models for Structural and Leak Transmission," J. Sound Vib., **230**(1), pp. 133–148.

[9] Hongisto, V., 2001, "A Case Study of Flanking Transmission Through Double Structures," Appl. Acoust., **62**(5), pp. 589–599.

[10] Wang, D.-W., Ma, L., Wen, Z.-H., and Glorieux, C., 2021, "Sound Transmission Loss of a Two-Layered Pyramidal Structure Lined With Porous Material," AIAA J., **59**(7), pp. 2714–2724.

[11] He, Z.-H., Wang, Y.-Z., and Wang, Y.-S., 2019, "Active Feedback Control on Sound Radiation of Elastic Wave Metamaterials," AIAA J., **57**(10), pp. 4536–4547.

[12] Shen, C., Xin, F., and Lu, T., 2016, "Sound Transmission Across Composite Laminate Sandwiches: Influence of Orthogonal Stiffeners and Laminate Layup," Compos. Struct., **143**, pp. 310–316.

[13] Wu, H., Hao, C., and Zhang, H., 2020, "Underwater Broadband Sound Insulation With Chiral Spiral Structures," AIP Adv., **10**(12), p. 125022.

[14] Duan, M., Yu, C., Xin, F., and Lu, T. J., 2021, "Tunable Underwater Acoustic Metamaterials Via Quasi-Helmholtz Resonance: From Low-Frequency to Ultra-Broadband," Appl. Phys. Lett., **118**(7), p. 071904.

[15] Chen, Y., Zhao, B., Liu, X., and Hu, G., 2020, "Highly Anisotropic Hexagonal Lattice Material for Low Frequency Water Sound Insulation," Extreme Mech. Lett., **40**, p. 100916.

[16] Panigrahi, S., Jog, C., and Munjal, M., 2008, "Multi-focus Design of Underwater Noise Control Linings Based on Finite Element Analysis," Appl. Acoust., **69**(12), pp. 1141–1153.

[17] Meng, H., Wen, J., Zhao, H., Lv, L., and Wen, X., 2012, "Analysis of Absorption Performances of Anechoic Layers With Steel Plate Backing," J. Acoust. Soc. Am., **132**(1), pp. 69–75.

[18] Cai, Z., Zhao, S., Huang, Z., Li, Z., Su, M., Zhang, Z., Zhao, Z., Hu, X., Wang, Y.-S., and Song, Y., 2019, "Bubble Architectures for Locally Resonant Acoustic Metamaterials," Adv. Funct. Mater., **29**(51), p. 1906984.

[19] Tong, L., Xiong, Z., Shen, Y.-X., Peng, Y.-G., Huang, X.-Y., Ye, L., Tang, M., et al., 2020, "An Acoustic Meta-Skin Insulator," Adv. Mater., **32**(37), p. 2002251.

[20] Huang, L., Xiao, Y., Wen, J., Zhang, H., and Wen, X., 2018, "Optimization of Decoupling Performance of Underwater Acoustic Coating With Cavities Via Equivalent Fluid Model," J. Sound Vib., **426**, pp. 244–257.

[21] Liu, H., Zhang, Q., Zhang, K., Hu, G., and Duan, H., 2019, "Designing 3D Digital Metamaterial for Elastic Waves: From Elastic Wave Polarizer to Vibration Control," Adv. Sci., **6**(16), p. 1900401.

[22] Wen, Z., Jin, Y., Gao, P., Zhuang, X., Rabczuk, T., and Djafari-Rouhani, B., 2022, "Topological Cavities in Phonic Plates for Robust Energy Harvesting," Mech. Syst. Signal Pr., **162**, p. 108047.

[23] Wang, Z., Zhang, Q., Zhang, K., and Hu, G., 2016, "Tunable Digital Metamaterial for Broadband Vibration Isolation at Low Frequency," Adv. Mater., **28**(44), pp. 9857–9861.

[24] Chen, Y., Zhang, Q., Zhang, Y., Xia, B., Liu, X., Zhou, X., Chen, C., and Hu, G., 2021, "Research Progress of Elastic Topological Materials," Adv. Mech., **51**(2), pp. 189–256.

[25] Yin, J., Cai, L., Fang, X., Xiao, Y., Yang, H., Zhang, H., Zhong, J., Zhao, H., Yu, D., and Wen, J., 2022, "Review on Research Progress of Mechanical Metamaterials and Their Applications on Vibration and Noise Control," Adv. Mech., **52**, pp. 1–79.

[26] Xiao, Y., and Wen, J., 2020, "Closed-Form Formulas for Bandgap Estimation and Design of Metastructures Undergoing Longitudinal or Torsional Vibration," J. Sound Vib., **485**, p. 115578.

[27] He, L., Wen, Z., Jin, Y., Torrent, D., Zhuang, X., and Rabczuk, T., 2021, "Inverse Design of Topological Metaplates for Flexural Waves With Machine Learning," Mater. Des., **199**, p. 109390.

[28] Zhong, H., Tian, Y., Gao, N., Lu, K., and Wu, J., 2021, "Ultra-Thin Composite Underwater Honeycomb-Type Acoustic Metamaterial With Broadband Sound Insulation and High Hydrostatic Pressure Resistance," Compos. Struct., **277**, p. 114603.

[29] Wei, Y., Liu, X., and Hu, G., 2021, "Quadramode Materials: Their Design Method and Wave Property," Mater. Des., **210**, p. 110031.

[30] Zhao, B., Wang, D., Zhou, P., Liu, X., and Hu, G., 2022, "Design of Load-Bearing Materials for Isolation of Low-Frequency Waterborne Sound," Phys. Rev. Appl., **17**(3), p. 034065.

[31] Wang, Y., Zhao, H., Yang, H., Liu, J., Yu, D., and Wen, J., 2022, "Topological Design of Lattice Materials With Application to Underwater Sound Insulation," Mech. Syst. Signal Pr., **171**, p. 108911.

[32] Ibrahim, R., 2008, "Recent Advances in Nonlinear Passive Vibration Isolators," J. Sound Vib., **314**(3–5), pp. 371–452.

[33] Wu, L., Wang, Y., Zhai, Z., Yang, Y., Krishnaraju, D., Lu, J., Wu, F., Wang, Q., and Jiang, H., 2020, "Mechanical Metamaterials for Full-Band Mechanical Wave Shielding," Appl. Mater. Today, **20**, p. 100671.

[34] Carrella, A., Brennan, M., Waters, T., and Lopes Jr, V., 2012, "Force and Displacement Transmissibility of a Nonlinear Isolator With High-Static-Low-Dynamic-Stiffness," Int. J. Mech. Sci., **55**(1), pp. 22–29.

[35] Le, T. D., and Ahn, K. K., 2011, "A Vibration Isolation System in Low Frequency Excitation Region Using Negative Stiffness Structure for Vehicle Seat," J. Sound Vib., **330**(26), pp. 6311–6335.

[36] Carrella, A., Brennan, M., Waters, T., and Shin, K., 2008, "On the Design of a High-Static–Low-Dynamic Stiffness Isolator Using Linear Mechanical Springs and Magnets," J. Sound Vib., **315**(3), pp. 712–720.

[37] Zhou, N., and Liu, K., 2010, "A Tunable High-Static–Low-Dynamic Stiffness Vibration Isolator," J. Sound Vib., **329**(9), pp. 1254–1273.

[38] Feng, X., and Jing, X., 2019, "Human Body Inspired Vibration Isolation: Beneficial Nonlinear Stiffness, Nonlinear Damping & Nonlinear Inertia," Mech. Syst. Signal Pr., **117**, pp. 786–812.

[39] Wang, Y., and Jing, X., 2019, "Nonlinear Stiffness and Dynamical Response Characteristics of an Asymmetric X-Shaped Structure," Mech. Syst. Signal Pr., **125**, pp. 142–169.

[40] Zhang, Q., Guo, D., and Hu, G., 2021, "Tailored Mechanical Metamaterials With Programmable Quasi-Zero Stiffness Features for Full-Band Vibration Isolation," Adv. Funct. Mater., **31**(33), p. 2101428.

[41] Zhou, J., Pan, H., Cai, C., and Xu, D., 2021, "Tunable Ultralow Frequency Wave Attenuations in One-Dimensional Quasi-Zero-Stiffness Metamaterial," Int. J. Mech. Mater. Des., **17**(2), pp. 285–300.

[42] Xin, F. X., and Lu, T. J., 2010, "Sound Radiation of Orthogonally Rib-Stiffened Sandwich Structures With Cavity Absorption," Compos. Sci. Technol., **70**(15), pp. 2198–2206.

[43] Wang, D.-W., and Ma, L., 2017, "Sound Transmission Through Composite Sandwich Plate With Pyramidal Truss Cores," Compos. Struct., **164**, pp. 104–117.

[44] Hughes, T. J., Cottrell, J. A., and Bazilevs, Y., 2005, "Isogeometric Analysis: CAD, Finite Elements, Nurbs, Exact Geometry and Mesh Refinement," Comput. Method. Appl. M., **194**(39–41), pp. 4135–4195.

[45] Wang, J., Lu, T. J., Woodhouse, J., Langley, R. S., and Evans, J., 2005, "Sound Transmission Through Lightweight Double-Leaf Partitions: Theoretical Modelling," J. Sound Vib., **286**(4–5), pp. 817–847.